The 2010 Maule, Chile earthquake: Downdip rupture limit revealed by space geodesy

Xiaopeng Tong,[1] David Sandwell,[1] Karen Luttrell,[1] Benjamin Brooks,[2] Michael Bevis,[3] Masanobu Shimada,[4] James Foster,[2] Robert Smalley Jr.,[5] Hector Parra,[6] Juan Carlos Báez Soto,[7] Mauro Blanco,[8] Eric Kendrick,[3] Jeff Genrich,[9] and Dana J. Caccamise II[3]

Received 14 October 2010; accepted 2 November 2010; published 30 December 2010.

[1] Radar interferometry from the ALOS satellite captured the coseismic ground deformation associated with the 2010 Mw 8.8 Maule, Chile earthquake. The ALOS interferograms reveal a sharp transition in fringe pattern at ~150 km from the trench axis that is diagnostic of the downdip rupture limit of the Maule earthquake. An elastic dislocation model based on ascending and descending ALOS interferograms and 13 near-field 3-component GPS measurements reveals that the coseismic slip decreases more or less linearly from a maximum of 17 m (along-strike average of 6.5 m) at 18 km depth to near zero at 43–48 km depth, quantitatively indicating the downdip limit of the seismogenic zone. The depth at which slip drops to near zero appears to be at the intersection of the subducting plate with the continental Moho. Our model also suggests that the depth where coseismic slip vanishes is nearly uniform along the strike direction for a rupture length of ~600 km. The average coseismic slip vector and the interseismic velocity vector are not parallel, which can be interpreted as a deficit in strike-slip moment release.
Citation: Tong, X., et al. (2010), The 2010 Maule, Chile earthquake: Downdip rupture limit revealed by space geodesy, *Geophys. Res. Lett.*, *37*, L24311, doi:10.1029/2010GL045805.

1. Introduction

[2] On February 27, 2010, a magnitude 8.8 earthquake struck off the coast of Maule, Chile. The earthquake occurred on a locked megathrust fault resulting from oblique convergence of the oceanic Nazca plate subducting beneath the continental South American plate at ~6.5 cm/yr [*Kendrick et al.*, 2003]. To date, the Maule event is the fifth largest earthquake since modern recording began, and the largest in this region since the great magnitude 9.5 Chile earthquake in 1960 [*National Earthquake Information Center* (*NEIC*), 2010]. Modern geodetic technologies permit this event to be studied in greater detail than was possible for any previous large earthquake. Studying the downdip limit of seismogenic rupture in relation to the compositional layering of surrounding areas may provide insights into the rheological controls on the earthquake process. Of particular interest in the case of continental subduction zones is the relationship between the downdip limit of stick-slip behavior and the depth of the continental Moho at its intersection with the subduction interface [*Oleskevich et al.*, 1999; *Hyndman*, 2007].

[3] There are at least four approaches to probing the downdip limit of seismic rupture for subduction thrust earthquakes. The first approach uses the maximum depth of the moderate thrust events along plate interfaces from global teleseismic data. *Tichelaar and Ruff* [1993] estimated the maximum depth of the seismically coupled zone of the Chile subduction zone to be 36–41 km south of 28°S and 48–53 km north of 28°S. Using a similar approach, *Pacheco et al.* [1993] suggested that this downdip limit is at 45 km depth in Central Chile. A second approach is to use the interseismic velocity from near-field GPS measurements to infer the downdip limit of the locked zone [*Brooks et al.*, 2003; *Bürgmann et al.*, 2005]. However, with the exceptions of Japan and Cascadia, there are generally not enough GPS stations in convergent plate boundaries to accurately constrain the locking depth. The third approach uses precisely located episodic-tremor-and-slip (ETS) (e.g., in Cascadia, southwest Japan, and Mexico) as a proxy for the downdip extent of the seismogenic zone [*Rogers and Dragert*, 2003; *Schwartz*, 2007]. A fourth approach uses geodetic measurements (e.g., GPS and InSAR) to invert for the co-seismic slip distribution on the megathrust and infer the downdip limit of the rupture [*Pritchard et al.*, 2007; *Hyndman*, 2007]. Here we use nearly complete geodetic coverage from ALOS L-band interferometry (launched January 2006) to resolve the spatial variations in slip for the entire Maule, Chile megathrust zone to a resolution of 40 km or better, and thus provide tight constraints on the depth of this rupture.

2. InSAR and GPS Data Analysis

[4] We investigated the crustal deformation produced by the M_w 8.8 Maule, Chile earthquake using interferometric synthetic aperture radar (InSAR) [*Massonnet and Feigl*, 1998] from the Advanced Land Observatory Satellite

[1]Scripps Instituion of Oceanography, University of California, San Diego, La Jolla, California, USA.
[2]School of Ocean and Earth Science and Technology, University of Hawaii, Honolulu, Hawaii, USA.
[3]School of Earth Sciences, Ohio State University, Columbus, Ohio, USA.
[4]Earth Observation Research Center, Japan Aerospace Exploration Agency, Tsukuba, Japan.
[5]Center for Earthquake Research and Information, University of Memphis, Memphis, Tennessee, USA.
[6]Instituto Geográfico Militar Chile, Santiago, Chile.
[7]Departamento de Ciencias Geodésicas y Geomática, Universidad de Concepción, Los Angeles, Chile.
[8]Instituto CEDIAC, Facultad de Ingeniería, Universidad Nacional de Cuyo, Mendoza, Argentina.
[9]Division of Geological and Planetary Sciences, California Institute of Technology, Pasadena, California, USA.

0094-8276/10/2010GL045805

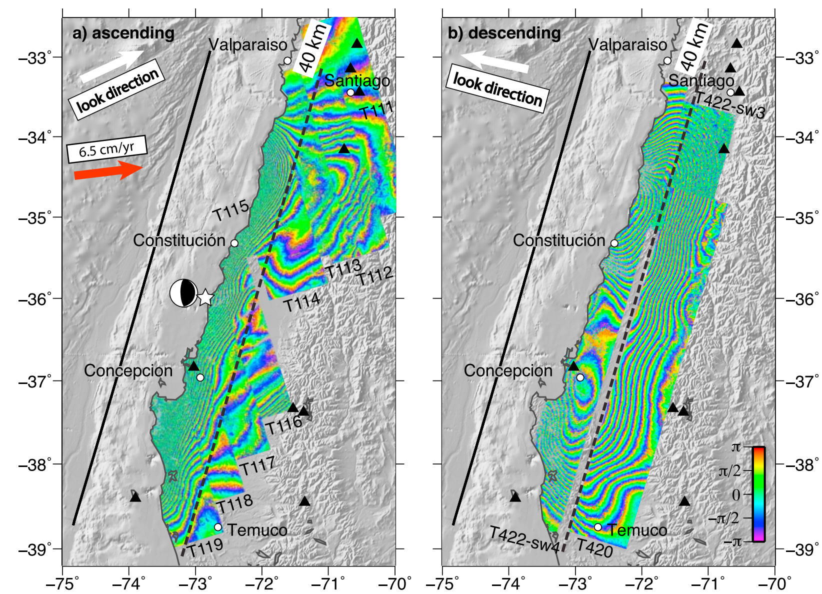

Figure 1. (a) Nine tracks of ascending interferograms (FBS-FBS mode) and (b) two tracks of descending interferograms (two subswaths of ScanSAR-ScanSAR mode and ScanSAR-FBS mode, and one track of FBS-FBS mode). The bold white arrow shows the horizontal component of the line of sight look direction. The nominal look angle from the vertical is 34°. The wrapped phase ($-\pi$ to π) corresponds a range change of 11.8 cm per cycle). The white star indicates the earthquake epicenter. The black triangles show the locations of the 13 GPS sites used in the inversion (4 sites are outside of the map boundaries). Solid black line shows the surface trace of the simplified fault model and the dashed black line marks the 40-km depth position of the fault for a 15° dip angle. The bold red arrow shows the interseismic convergence vector.

(ALOS) [*Shimada et al.*, 2010] in conjunction with measurements obtained from thirteen continuously operating GPS (CGPS) stations (see auxiliary material).[1] Following the Maule, Chile earthquake, the Japan Aerospace Exploration Agency (JAXA) conducted high priority observations using Fine Beam Single Polarization (FBS) strip-mode SAR along ascending orbits and burst-synchronized ScanSAR along descending orbits. The improved coherence at L-band along with systematic pre- and post-earthquake acquisitions yielded excellent coseismic InSAR coverage of a 630 km by 150 km area of ground deformation (Figure 1). The interferograms were analyzed frame-by-frame using the same local earth radius and spacecraft ephemeris to ensure along-track phase continuity (see Table S2 of the auxiliary material). We used the line-of-sight (LOS) displacement from both ascending and descending orbits to distinguish between horizontal and vertical deformation. We processed track T422-subswath4 (T422-sw4) using newly developed FBS to ScanSAR software following the algorithm of *Ortiz and Zebker* [2007] and track T422-subswath3 (T422-sw3) using our ScanSAR-ScanSAR processor, which is part of the GMTSAR software [*Sandwell et al.*, 2008; *Tong et al.*, 2010]. The ScanSAR to strip mode interferograms along track T422-sw4 are critical for recovering the complicated deformation near the shoreline from the descending orbits.

[5] An examination of the raw phase data reveals an interesting feature in the coseismic surface deformation: the dashed black line on the ascending interferograms (Figure 1a) marks a boundary where the phase gradient changes remarkably, reflecting that the coseismic slip stopped at ~150 km from the trench axis (i.e., ~40 km depth for a fault with 15° dip angle). At a similar distance from the trench, the descending interferograms exhibit a phase minimum (Figure 1b). Both of these features are diagnostic of the surface deformation immediately above the downdip extent of the megathrust [*Savage*, 1983]. The different signatures seen in the ascending and descending interferograms are due to the difference in the radar LOS vectors.

[6] As interferograms are only able to detect relative movement, GPS vectors are important for providing absolute measurements of displacement and constraining the overall magnitude of slip [*Fialko et al.*, 2001]. Near-field 3-component GPS displacement vectors in this region provide independent constraints on the fault slip model. We did not include GPS measurements that are beyond ~300 km from the coast of the Maule, Chile region. Adding the far-field GPS sites should not change the features of our slip model in the depth of 15–45 km because the geometric attenuation would cause all the far-field GPS measurements to be largely sensitive to the long wavelength part of the model. Methods used for unwrapping the interferograms and adjusting the absolute value of range change to the GPS measurements are discussed in the auxiliary material. We found that it was not necessary to remove a ramp from the interferograms in order to achieve the 10 cm uncertainty assigned to the digitized InSAR measurements.

[7] The LOS displacement ranges from 1 cm to 418 cm along ascending orbits (820 data points) and −374 cm to 15 cm along descending orbits (1112 data points). The maximum LOS displacement along the ascending tracks is near the Peninsula in Arauco, Chile while the maximum negative LOS displacement along the descending track is north of Constitución (see Figure S1 of the auxiliary material). Profiles of LOS displacement (Figures S2a and S2b) show that the characteristic inflection points at

[1]Auxiliary materials are available in the HTML. doi:10.1029/2010GL045805.

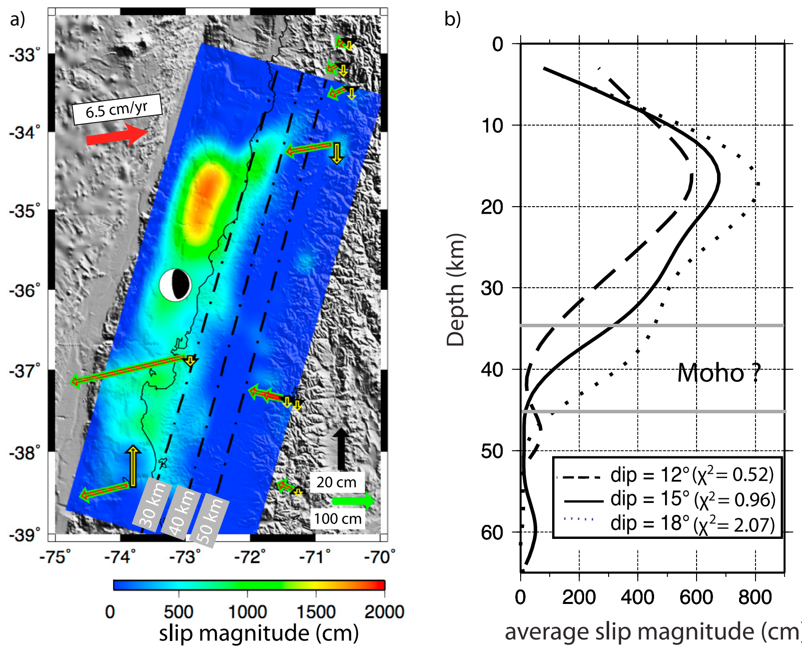

Figure 2. (a) Coseismic slip model along a 15° dipping fault plane over shaded topography in Mercator projection. Dashed lines show contours of fault depth. The fat green and black arrows show the observed horizontal and vertical displacement of the GPS vectors respectively and the narrow red and yellow arrows show the predicted horizontal and vertical displacement. (b) Averaged slip versus depth for different dip angles. Data misfits are shown in the parentheses (see text).

~150 km east of the trench are readily discernable from transects of the InSAR LOS displacement.

3. Coseismic Slip Model and Resolution Test

[8] We used InSAR and GPS observations to constrain a model of coseismic slip on a single plane striking N 16.8°E and dipping 15° to the east, approximating the geometry of the megathrust (Figure 2a). We also tested a model that more closely follows the trench axis, but the more complicated model did not improve the RMS misfit. The surface trace and dip angle of the fault plane were initially determined by fitting the locations of M > 6.0 aftershocks [*NEIC*, 2010] and then refined using the geodetic data. The weighted residual misfit is determined from $\chi^2 = \frac{1}{N}\sum_{i=1}^{N}\left(\frac{o_i - m_i}{\sigma_i}\right)^2$, where o_i is the geodetic displacement measurement, m_i is the modeled displacement, σ_i is the uncertainty estimate of the i^{th} measurement, and N is the total number of InSAR LOS displacement and 3-component GPS measurements. A 15° dip is preferred because a steeper dip angle (18°) results in a larger misfit (Figure 2b) and a shallower dip angle (12°) results in unlikely maximum slip at the top edge of the fault plane (i.e., 0 km depth). Moreover, the 12° dipping fault plane lies shallower than both the hypocenter and the M > 4 background seismicity from 1960–2007, whose depths are well constrained in the EHB bulletin [*International Seismological Centre*, 2009] (Figure S2d).

[9] This finite fault model assumes an isotropic homogeneous elastic half-space [*Fialko*, 2004; *Okada*, 1985]. Details of the modeling approach are provided in the auxiliary material. The RMS misfit for ascending and descending LOS displacement is 10.9 cm and 7.9 cm respectively and the RMS misfit for the GPS data is: 1.54 cm for the east component, 0.44 cm for the north component and 2.93 cm for the up component. The residuals in InSAR LOS displacement (see Figures S1c and S1d of the auxiliary material) are generally smaller than 15 cm, though there are larger misfits in the southern end of the rupture area. The ALOS interferograms, LOS data points and slip model are available at ftp://topex.ucsd.edu/pub/chile_eq/.

[10] The preferred slip model (Figure 2a) shows significant along-strike variation of the fault rupture. The most intense fault slip is found to be about 17 m, located at 120–160 km north of the epicenter. This is consistent with the large LOS displacement over that region seen in the interferograms (Figure 1). To the south of the epicenter near the peninsula in Arauco, Chile is another patch of significant slip. The length of the rupture area of slip greater than one meter is 606 km, compared with 645 km indicated by the aftershock distribution [*NEIC*, 2010]. Figure 2b shows the depth distribution of fault slip from the geodetic inversion. The peak of the coseismic slip is located offshore and is at ~18 km depth. The depth of maximum slip is slightly shallower than the depth of rupture initiation, given by the PDE catalog as 22 km [*NEIC*, 2010].

[11] The coseismic slip model from a joint inversion of GPS and InSAR data (Figure 2a) suggests the slip direction is dominantly downdip, with a relatively small component of right-lateral strike slip. Assuming the average shear modulus to be 40 GPa (see auxiliary material), the total moment of the preferred model is 1.82×10^{22} Nm (thrust component: 1.68×10^{22} Nm; right-lateral strike-slip component: 4.89×10^{21} Nm). The total corresponds to moment magnitude 8.77, comparable to the seismic moment magnitude 8.8 [*NEIC*, 2010]. Because of the lack of observations offshore, the geodetic model probably underestimates the amount of slip at shallower depth, which could explain the

observed moment discrepancy. The above relatively smooth and simple model results in a variance reduction in the geodetic data of 99%.

[12] We compared the direction of the interseismic velocity vector with the direction of the area-averaged coseismic slip vector. A non-parallel interseismic velocity vector and coseismic slip vector would indicate an incomplete moment release of the Maule event. The interseismic velocity from the Nazca-South America Euler vector is oriented at 27.3° counterclockwise from trench perpendicular [*Kendrick et al.* 2003]. Based on the ratio of the thrust and right-lateral strike-slip moments, the area-averaged coseismic slip direction is 16.8° counterclockwise from trench perpendicular. The misalignment of the interseismic velocity vector and the coseismic slip vector could be interpreted as a moment deficit in right-lateral strike-slip moment. This moment deficit is about 3.49×10^{21} Nm, equivalent to 70% of the moment release in strike-slip component, which could be accommodated by either aseismic slip or subsequent earthquakes.

[13] The most intriguing observation from the slip model is that the along-strike-averaged slip decreases by more than a factor of 10 between 18 km and 43 km depth and reaches a minimum of approximately zero at a depth of 43–48 km (Figure 2b). This dramatic decrease indicates the downdip limit of the seismogenic zone and the transition from seismic to aseismic slip. In addition we note a depth range where the coseismic slip deviates from a linear decrease and somewhat flattens at 30–35 km depth. This deviation at 30–35 km depth resembles the "plateau" of the interseismic coupling at Nakai Trough, Japan [*Aoki and Scholz*, 2003]. The depth at which slip drops to near zero is almost uniform in the along-strike direction for a rupture length of ~600 km. This depth approximately corresponds to the intersection of the subducting plate with the continental Moho. Based on receiver function and seismic refraction analysis, the Moho depth is between 35 and 45 km [*Yuan et al.*, 2002; *Sick et al.*, 2006], although it is not well resolved at its intersection with the subducting plate.

[14] We used a checkerboard resolution test to explore the model resolution (see auxiliary material) and found that features of 40 km by 40 km are well resolved over the area of InSAR coverage, which provides approximately 10 km absolute depth resolution along the dipping fault plane (see Figure 2b). Slip uncertainties are larger at the top and bottom ends of the fault plane (depth < 15 km and depth > 50 km). The slip model also shows a slight increase in slip at depth greater than 50 km, but this feature is not supported by the resolution analysis.

4. Discussion and Conclusions

[15] We compared the coseismic slip model derived from near-field displacement measurements from this study with previous published slip models. Our geodetic inversion, a teleseismic inversion of P, SH, and Rayleigh wave [*Lay et al.*, 2010] and a joint inversion of InSAR, GPS, and teleseismic data [*Delouis et al.*, 2010] all suggest that the largest slip occurred to the north of the epicenter. However, none of the previous studies have used the InSAR observations from both the ascending and descending orbits to resolve the downdip rupture limit. Our study is novel in that we infer the downdip rupture limit from a prominent change in LOS displacement manifested in interferograms (Figure 1).

[16] The along-strike averaged slip depth distribution suggests that the coseismic slip of the Maule event peaks at 18 km depth and decreases to near zero at 43–48 km depth. From a phenomenological perspective the slip distribution indicates that the contact between oceanic and continental crust is velocity weakening. The largest fraction of interseismic coupling occurs at a depth of ~18 km and this fraction decreases more or less linearly with increasing depth to ~43 km where it becomes essentially zero. This observation is in fair agreement with the observation that earthquake depth distribution tapers smoothly to zero [*Tichelaar and Ruff*, 1993; *Pacheco et al.*, 1993], indicating the accumulated and released energy on the megathrust is not a simple step function that goes to zero at 43 km.

[17] Based on available seismic evidence on the local Moho depth, we note that the downdip coseismic rupture limit is near the depth where the subducting Nazca plate intersects with the continental Moho of the South America plate. This downdip limit approximately coincides with the transition in topography from Coast Range to Longitudinal Valley. It is noticeable that the free-air gravity changes from positive to negative at similar location as this downdip limit (see Figure S2c).

[18] There are two possible physical mechanisms controlling the downdip limit of the seismogenic zone. First, fault friction behavior may transition from velocity weakening to velocity strengthening at the depth of the 350–450°C isotherm [*Oleskevich et al.*, 1999; *Hyndman*, 2007; *Klingelhoefer et al.*, 2010]. Second, the downdip rupture limit may occur at the depth of the fore-arc Moho due to a change in frictional properties associated with the serpentinization of the mantle wedge [*Bostock et al.* 2002; *Hippchen and Hyndman*, 2008]. In southern Chile, the 350°C isotherm is at a similar depth as the fore-arc Moho, hence previous studies could not distinguish between the two possible controlling mechanisms [*Oleskevich et al.*, 1999]. The observed monotonic decrease in slip with depth combined with the tapering of the earthquake depth distribution provides new information that can be used to constrain earthquake cycle models at megathrusts. This transitional behavior is similar to what is observed on continental transform faults both in terms of coseismic slip [*Fialko et al.*, 2005] and seismicity [*Marone and Scholz*, 1988].

[19] In summary we have found: (1) The ALOS interferograms show pronounced changes in fringe pattern at a distance of ~150 km from the trench axis that are diagnostic of the downdip rupture limit of the Maule earthquake. (2) An elastic dislocation model based on InSAR and GPS displacement measurements shows that the coseismic slip decreases more or less linearly from its maximum at ~18 km depth to near zero at ~43 km depth. (3) The depth at which slip drops to near zero is almost uniform in the along-strike direction for a rupture length of ~600 km and it appears to be at the intersection of the subducting plate with the continental Moho. (4) The average coseismic slip vector and the interseismic velocity vector are not parallel, suggesting a possible deficit in strike-slip moment release.

[20] **Acknowledgments.** This work is supported by the National Science Foundation Geophysics Program (EAR 0811772) and the NASA Geodetic Imaging Program (NNX09AD12G). Research for this project at the Caltech Tectonic Observatory was supported by the Gordon and Betty Moore Foundation.

References

Aoki, Y., and C. H. Scholz (2003), Interseismic deformation at the Nankai subduction zone and the Median Tectonic Line, southwest Japan, *J. Geophys. Res.*, *108*(B10), 2470, doi:10.1029/2003JB002441.

Bostock, M. G., et al. (2002), An inverted continental Moho and serpentinization of the forearc mantle, *Nature*, *417*, 536–538, doi:10.1038/417536a.

Brooks, B. A., M. Bevis, R. Smalley Jr., E. Kendrick, R. Manceda, E. Lauría, R. Maturana, and M. Araujo (2003), Crustal motion in the Southern Andes (26°–36°S): Do the Andes behave like a microplate?, *Geochem. Geophys. Geosyst.*, *4*(10), 1085, doi:10.1029/2003GC000505.

Bürgmann, R., M. G. Kogan, G. M. Steblov, G. Hilley, V. E. Levin, and E. Apel (2005), Interseismic coupling and asperity distribution along the Kamchatka subduction zone, *J. Geophys. Res.*, *110*, B07405, doi:10.1029/2005JB003648.

Delouis, B., J.-M. Nocquet, and M. Vallée (2010), Slip distribution of the February 27, 2010 Mw = 8.8 Maule earthquake, central Chile, from static and high-rate GPS, InSAR, and broadband teleseismic data, *Geophys. Res. Lett.*, *37*, L17305, doi:10.1029/2010GL043899.

Fialko, Y. (2004), Probing the mechanical properties of seismically active crust with space geodesy: Study of the coseismic deformation due to the 1992 M(w)7.3 Landers (southern California) earthquake, *J. Geophys. Res.*, *109*, B03307, doi:10.1029/2003JB002756.

Fialko, Y., M. Simons, and D. Agnew (2001), The complete (3-D) surface displacement field in the epicentral area of the 1999 M(w)7.1 Hector Mine earthquake, California, from space geodetic observations, *Geophys. Res. Lett.*, *28*(16), 3063–3066, doi:10.1029/2001GL013174.

Fialko, Y., et al. (2005), Three-dimensional deformation caused by the Bam, Iran, earthquake and the origin of shallow slip deficit, *Nature*, *435*, 295–299, doi:10.1038/nature03425.

Hippchen, S., and R. D. Hyndman (2008), Thermal and structural models of the Sumatra subduction zone: Implications for the megathrust seismogenic zone, *J. Geophys. Res.*, *113*, B12103, doi:10.1029/2008JB005698.

Hyndman, R. D. (2007), The seismogenic zone of subduction thrust faults: What we know and don't know, in *The Seismogenic Zone of Subduction Thrust Faults*, edited by T. H. Dixon and J. C. Moore, pp. 15–35, Columbia Univ. Press, New York.

International Seismological Centre (2009), EHB Bulletin, Int. Seismol. Cent., Thatcham, U. K. (Available at http://www.isc.ac.uk)

Kendrick, E., et al. (2003), The Nazca–South America Euler vector and its rate of change, *J. South Am. Earth Sci.*, *16*(2), 125–131, doi:10.1016/S0895-9811(03)00028-2.

Klingelhoefer, F., M.-A. Gutscher, S. Ladage, J.-X. Dessa, D. Graindorge, D. Franke, C. André, H. Permana, T. Yudistira, and A. Chauhan (2010), Limits of the seismogenic zone in the epicentral region of the 26 December 2004 great Sumatra-Andaman earthquake: Results from seismic refraction and wide-angle reflection surveys and thermal modeling, *J. Geophys. Res.*, *115*, B01304, doi:10.1029/2009JB006569.

Lay, T., C. J. Ammon, H. Kanamori, K. D. Koper, O. Sufri, and A. R. Hutko (2010), Teleseismic inversion for rupture process of the 27 February 2010 Chile (Mw 8.8) earthquake, *Geophys. Res. Lett.*, *37*, L13301, doi:10.1029/2010GL043379.

Marone, C., and C. H. Scholz (1988), The depth of seismic faulting and the upper transition from stable to unstable slip regimes, *Geophys. Res. Lett.*, *15*, 621–624, doi:10.1029/GL015i006p00621.

Massonnet, D., and K. L. Feigl (1998), Radar interferometry and its application to changes in the earth's surface, *Rev. Geophys.*, *36*(4), 441–500, doi:10.1029/97RG03139.

National Earthquake Information Center (NEIC) (2010), Magnitude 8.8—Offshore Maule, Chile, U. S. Geol. Surv., Denver, Colo. (Available at http://earthquake.usgs.gov/earthquakes/recenteqsww/Quakes/us2010tfan.php)

Okada, Y. (1985), Surface deformation due to shear and tensile faults in a half-space, *Bull. Seismol. Soc. Am.*, *75*(4), 1135–1154.

Oleskevich, D., R. D. Hyndman, and K. Wang (1999), The updip and downdip limits of subduction earthquakes: Thermal and structural models of Cascadia, south Alaska, S.W. Japan, and Chile, *J. Geophys. Res.*, *104*, 14,965–14,991, doi:10.1029/1999JB900060.

Ortiz, A. B., and H. Zebker (2007), ScanSAR-to-stripmap mode interferometry processing using ENVISAT/ASAR data, *IEEE Trans. Geosci. Remote Sens.*, *45*(11), 3468–3480, doi:10.1109/TGRS.2007.895970.

Pacheco, J. F., L. R. Sykes, and C. H. Scholz (1993), Nature of seismic coupling along simple plate boundaries of the subduction type, *J. Geophys. Res.*, *98*(B8), 14,133–14,159, doi:10.1029/93JB00349.

Pritchard, M. E., E. O. Norabuena, C. Ji, R. Boroschek, D. Comte, M. Simons, T. H. Dixon, and P. A. Rosen (2007), Geodetic, teleseismic, and strong motion constraints on slip from recent southern Peru subduction zone earthquakes, *J. Geophys. Res.*, *112*, B03307, doi:10.1029/2006JB004294.

Rogers, G., and H. Dragert (2003), Episodic tremor and slip on the Cascadia subduction zone: The chatter of silent slip, *Science*, *300*(5627), 1942–1943, doi:10.1126/science.1084783.

Sandwell, D. T., et al. (2008), Accuracy and resolution of ALOS interferometry: Vector deformation maps of the Father's Day intrusion at Kilauea, *IEEE Trans. Geosci. Remote Sens.*, *46*(11), 3524–3534, doi:10.1109/TGRS.2008.2000634.

Savage, J. C. (1983), A dislocation model of strain accumulation and release at a subduction zone, *J. Geophys. Res.*, *88*(B6), 4984–4996, doi:10.1029/JB088iB06p04984.

Schwartz, S. Y. (2007), Episodic aseismic slip at plate boundaries, in *The Treatise on Geophysics*, vol. 4, *Earthquake Seismology*, edited by G. Schubert, pp. 445–472, doi:10.1016/B978-044452748-6.00076-6, Elsevier, Amsterdam.

Shimada, M., T. Tadonoand, and A. Rosenqvist (2010), Advanced Land Observing Satellite (ALOS) and Monitoring Global Environmental Change, *Proc. IEEE*, *98*(5), 780–799, doi:10.1109/JPROC.2009.2033724.

Sick, C., et al. (2006), Seismic images of accretive and erosive subduction zones from the Chilean margin, in *The Andes*, edited by O. Oncken et al., pp. 147–169, doi:10.1007/978-3-540-48684-8_7, Springer, Berlin.

Tichelaar, B. W., and L. J. Ruff (1993), Depth of seismic coupling along subduction zones, *J. Geophys. Res.*, *98*(B2), 2017–2037, doi:10.1029/92JB02045.

Tong, X., D. T. Sandwell, and Y. Fialko (2010), Coseismic slip model of the 2008 Wenchuan earthquake derived from joint inversion of interferometric synthetic aperture radar, GPS, and field data, *J. Geophys. Res.*, *115*, B04314, doi:10.1029/2009JB006625.

Yuan, X., S. V. Sobolev, and R. Kind (2002), Moho topography in the central Andes and its geodynamic implications, *Earth Planet. Sci. Lett.*, *199*(3–4), 389–402, doi:10.1016/S0012-821X(02)00589-7.

J. C. Báez Soto, Departamento de Ciencias Geodésicas y Geomática, Universidad de Concepción, Campus Los Angeles, J. A. Coloma 0201, Los Angeles 445-1032, Chile.

M. Bevis, D. J. Caccamise II, and E. Kendrick, School of Earth Sciences, Ohio State University, 275 Mendenhall Laboratory, 125 South Oval, Columbus, OH 43210, USA.

M. Blanco, Instituto CEDIAC, Facultad de Ingeniería, Universidad Nacional de Cuyo, Parque General San Martín, Mendoza 405-5500, Argentina.

B. Brooks and J. Foster, School of Ocean and Earth Science and Technology, University of Hawaii, 1680 East West Rd., Honolulu, HI 96822, USA.

J. Genrich, Division of Geological and Planetary Sciences, California Institute of Technology, MC 100-23, 272 South Mudd Laboratory, Pasadena, CA 91125, USA.

K. Luttrell, D. Sandwell, and X. Tong, Scripps Instituion of Oceanography, University of California, San Diego, La Jolla, CA 92093-0225, USA. (ttxxpp@gmail.com)

H. Parra, Instituto Geográfico Militar Chile, Nueva Santa Isabel 1640, Santiago, Chile.

M. Shimada, Earth Observation Research Center, Japan Aerospace Exploration Agency, Sengen 2-1-1, Tsukuba, Ibaraki 350-8505, Japan.

R. Smalley Jr., Center for Earthquake Research and Information, University of Memphis, 3876 Central Ave., Ste. 1, Memphis, TN 38152-3050, USA.

Auxiliary Material for "The 2010 Maule, Chile earthquake: Downdip rupture limit revealed by space geodesy"

Xiaopeng Tong[1], David Sandwell[1], Karen Luttrell[1], Benjamin Brooks[2], Michael Bevis[3], Masanobu Shimada[4], James Foster[2], Robert Smalley Jr.[5], Hector Parra[6], Juan Carlos Báez Soto[7], Mauro Blanco[8], Eric Kendrick[3], Jeff Genrich[9], Dana J. Caccamise II[3]

[1]Scripps Institution of Oceanography, University of California San Diego, La Jolla, CA 92093-0225 USA

[2]Hawaii Institutes of Geophysics and Planetology, University of Hawaii, Honolulu, HI 96822 USA

[3]School of Earth Science, Ohio State University, 125 South Oval 275 Mendenhall Laboratory, Columbus, OH 43210, USA

[4]Japan Aerospace Exploration Agency, Earth Observation Research Center, Tsukuba Ibaraki, 350-8505, Japan

[5]Center for Earthquake Research and Information, University of Memphis, 3876 Central Ave Ste 1, Memphis, TN, 38152-3050, USA

[6]Instituto Geográfico Militar Chile, Dieciocho No 369, Santiago, Chile.

[7]Universidad de Concepción, Campus Los Angeles, J. A. Coloma 0201, Los Angeles, Chile

[8]Instituto CEDIAC, Facultad de Ingeniería, Universidad Nacional de Cuyo, CC405 CP5500, Mendoza, Argentina

[9]Division of Geological and Planetary Science, California Institute of Technology, Pasadena, CA 91125 US

This supplementary material provides details on the GPS and InSAR data analysis, including the temporal and spatial coverage of the InSAR and GPS data, data misfit and inversion method (see Table S1 and Table S2). The radar line-of-sight displacement measurements and their residuals are summarized in Figure S1 and S2. Our conclusions regarding the variations in slip with depth and the estimate of near-zero slip below ~45 km depth depend on the coverage and accuracy of the geodetic data as well as the characteristics of the model. We investigated the effects of the smoothness parameter on the spatial resolution of the model (see Figure S3). In addition, the supplementary material describes our inversion method and synthetic resolution tests in greater detail to assist the evaluation of the slip model (see Figure S4, S5, S6).

GPS Data Analysis

All available continuous GPS data in South America from 2007 through 2010 May 5 were processed using GAMIT [*King and Bock*, 2000] with additional GPS sites included to provide reference frame stability (Table S1). All data were processed using the MIT precise orbits. Orbits were held tightly constrained and standard earth orientation parameters (EOP) and earth and ocean tides were applied. Due to the number of stations, two separate subnets were formed with common fiducial sites. The subnets were merged and combined with MIT's global solution using GLOBK. We defined a South American fixed reference frame, primarily from the Brazilian craton, to better than 2.4 mm/yr RMS horizontal velocity by performing daily Helmert transformations for the network solutions and stacking in an ITRF2005 reference frame [*Kendrick, et al.*, 2006]. Finally we used these time series to estimate the coseismic displacement, or jumps, at each station affected by the Maule event, as well as crustal velocity before and after the earthquake.

InSAR Phase Unwrapping and Adjustment

We unwrapped all the interferograms by digitizing and counting fringes at every 2π phase cycle (11.8 cm) (see Figure S1) [*Tong et al.*, 2010]. This method works well even in low coherence areas, such as ScanSAR-ScanSAR interferograms (see Figure 1, T422-sw3). We assembled all the digitized fringes, subsampled them using a blockmedian average with pixel spacing of 0.05° in latitude and 0.1° in longitude, and converted them into line of sight (LOS) displacement. The interferograms are subject to propagation delay through the atmosphere and ionosphere. It is likely that T112 and parts of T116 include significant (> 10 cm) ionospheric delay, so these data were excluded from the analysis (see Figure S1a and Table S2). To account for the potential errors in digitization and propagation delay effects, we assigned a uniform uncertainty of 10 cm to the LOS data. Interferometry is a relative measurement of LOS displacement, so after unwrapping the average value of each track was adjusted to match the available GPS displacement vectors projected into the LOS direction. For tracks that do not contain a GPS station, their average value was adjusted so that the LOS displacement field is mostly continuous from track to track. Over a distance of up to 1000 km the satellite orbits are much more accurate than the 10 cm assigned uncertainty [*Sandwell et al.*, 2008] so no linear ramp was removed from the unwrapped and sampled LOS displacement data. Even after adjustment, the phase between neighboring tracks is sometimes discontinuous, as seen, for example, at the southern end of the descending interferograms (see Figure 1b and Figure S1b) where the fringes are denser in T422-sw4 than T420. This is partially due to the difference in look angle between the far range in one track and the near range of the adjacent track. This kind of discontinuity can also be caused by rapid and significant postseismic deformation between the acquisition times of the adjacent SAR tracks. The final step in the processing was to calculate the unit look vector between each LOS data point and the satellite using the precise orbits. This is needed to project the vector deformation from a model into the LOS direction of the measurement.

Uncertainty in GPS and InSAR data

When calculating the weighted residual misfit, we estimated the uncertainty of the geodetic measurement. Errors in the GPS measurement were calculated using residual scatter values (Table S1). Errors in the InSAR LOS displacement measurement were assigned uniformly as 10 cm based on posteriori misfit.

Model optimization

The model consists of a 670 km long and 260 km wide 15° dipping fault plane in a homogeneous elastic half-space (Figure S3). The fault plane is subdivided into 19.7 km by 20 km patches. The fault patch size was chosen to retrieve major features in the slip model while keeping the inversion problem manageable. We applied a non-negativity constraint to allow only thrust and right-lateral strike slip; only the bottom boundary of the fault plane is constrained to have zero slip. The minimization criteria is given by the equation

$$\min(\|Am - b\|^2 + \lambda^2 \|Sm\|^2) \qquad (1)$$

where the first term minimizes the data misfit and the second term minimizes model roughness (i.e., second derivative) of slip on the fault plane. In the first term, A is the inversion matrix, m is the vector of unknowns, and b is the matrix of observations, given by

$$A = \begin{bmatrix} \sigma_{LOS}{}^{-1} G_{LOS} \\ \beta \sigma_{GPS}{}^{-1} G_{GPS} \end{bmatrix},\ m = \begin{bmatrix} m_{dip} \\ m_{strike} \end{bmatrix},\ b = \begin{bmatrix} \sigma_{LOS}{}^{-1} d_{LOS} \\ \beta \sigma_{GPS}{}^{-1} d_{GPS} \end{bmatrix} \qquad (2)$$

The A matrix consists of the Green's function matrices G_{LOS} and G_{GPS} weighted by the uncertainties in the measurements. The two diagonal matrices σ_{LOS} and σ_{GPS} are derived from measurement uncertainties, and β represents the relative weight between InSAR and GPS data sets. The model vectors m_{dip} and m_{strike} represent dip-slip components and strike-slip components on discretized fault patches. In matrix b, the observation vectors d_{LOS} and d_{GPS} consist of the InSAR data, which are the LOS displacement from the ascending and descending tracks, and the GPS data with east-north-up displacement components. In the second term the smoothness matrix is given by

$$S = \begin{pmatrix} -1 & 4 & -1 & 0 & \dots \\ 0 & -1 & 4 & -1 & \dots \\ 0 & 0 & -1 & 4 & -1 \\ \dots & \dots & \dots & \dots & \dots \end{pmatrix}. \qquad (3)$$

The relative weighting between GPS and InSAR data, parameter β, is determined iteratively so that the residuals are minimized in both datasets. We select the relative weighting between the data misfit and roughness, parameter λ, based on the trade-off curve between model smoothness and the normalized RMS misfit. Nine different weights were tested and the preferred model is chosen at the turning point of this trade-off curve (Figure S3). While the selection of the best model is somewhat subjective, all the models share a common characteristic of high depth-averaged slip at an along-dip distance of 60-100 km and essentially zero slip at ~160 km.

Resolution tests

To assess the resolution capabilities of the data and model, we conducted two sets of checkerboard tests. The first test had a 20 km checkerboard of 500 cm in dip slip (Figure S4). The checkerboard model was used to generate synthetic InSAR and GPS data at the observation locations. The InSAR, and GPS data were assigned the same uncertainties as used in the final model. We inverted for a best fitting solution by adjusting the smoothness parameter while retaining all the other parameter settings as were used in the final model (Figure S4).

We found that the resolution is better over the southern half of the fault plane where there is more complete InSAR coverage closer to the trench axis. We calculated the RMS of the slip difference (i.e. a measure of the misfit) between the synthetic model and the recovered model, averaged over the fault strike direction. Plots of RMS slip difference versus depth (Figure S6) show a minimum at a downdip distance of 120 km. The accuracy of the recovered model is good between downdip distances of 110 and 130 km where the average RMS curve falls below 100 cm. Over this depth range features as small as 20 km can be resolved to a 20% accuracy.

We repeated the checkerboard test at a size of 40 km as shown in Figure S5. The accuracy of the recovered checkerboard improves significantly when the checker size is increased from 20 km to 40 km. We calculated the RMS of the slip difference in the same way as for the 20 km checker size (see Figure S6). The accuracy of the recovered model is good between downdip distances of 70 and 220 km where the average RMS curve falls below 100 cm, corresponding to the area where the recovered model uncertainties are less than 20% of the input model. The accuracy is excellent between the downdip distances of 80 and 190 km where the average RMS curve falls below 50 cm, corresponding to the area where the recovered model uncertainties are less than 10% of the input model. From these checkerboard tests we conclude that the overall model resolution is 40 km or better over the downdip width range of 70 to 220 km.

Determination of shear modulus

Our model requires a representative value of shear modulus in order to calculate the geodetic moments from the slip model, although the Okada's displacement solution only depends on the Poisson's ratio. We determined the average shear modulus from regional 1D seismic velocity structure [*Bohm et al*., 2002]. Above 45 km depth, the average shear modulus (weighted by layer thickness) is 38.3 GPa. Above 55km depth, the average shear modulus (weighted by layer thickness) is 43.5 GPa. Thus an average shear modulus of 40 GPa is a preferred value for estimating geodetic moment (Table S3).

Supplementary References

Bohm, M., et al., (2002), The Southern Andes between 36° and 40° latitude: seismicity and average seismic velocities. Tectonophys, 356(4):275–289

Kendrick, E., et al. (2006), Active Orogeny of the South-Central Andes Studied With GPS Geodesy, Revista de la Asociación Geológica Argentina, 61 (4), 555-566

King, R., and Y. Bock (2000), Documentation for the GAMIT GPS Analysis Software, Massachusetts Institute of Technology and Scripps Institute of Oceanography, Cambridge, Mass.

Sandwell, D.T., et al. (2008), Accuracy and Resolution of ALOS Interferometry: Vector Deformation Maps of the Father's Day Intrusion at Kilauea, IEEE Trans. Geosci. Remote Sens., 46(11), 3524-3534.

Tong, X., D. T. Sandwell and Y. Fialko (2010), Coseismic slip model of the 2008 Wenchuan earthquake derived from joint inversion of interferometric synthetic aperture radar, GPS, and field data, J. Geophys. Res., 115, B04314, doi:10.1029/2009JB006625.

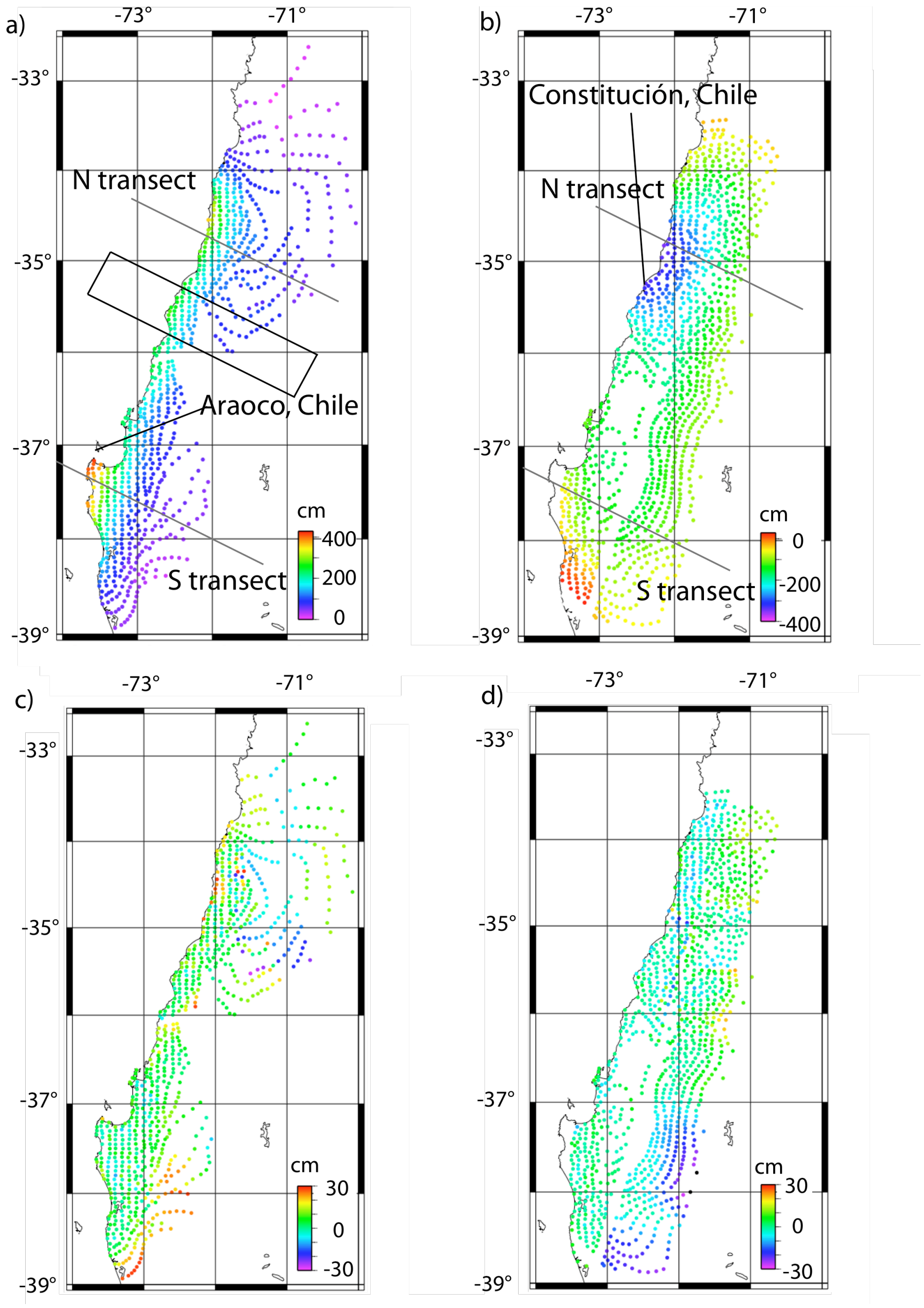

Figure S1. Unwrapped, subsampled, and calibrated InSAR line-of-sight (LOS) displacements and their residuals. Positive LOS displacement indicates ground motion toward the radar. a) Ascending LOS displacement. b) Descending LOS displacement. c) Model residuals of the ascending LOS displacement. d) Model residual of the descending LOS displacement. The two black lines (N transect and S transect) mark the locations of profiles shown in Figure 2a and Figure 2b. The black box in subplot a) shows the sampled area of topography and gravity profiles as shown in Figure S2c.

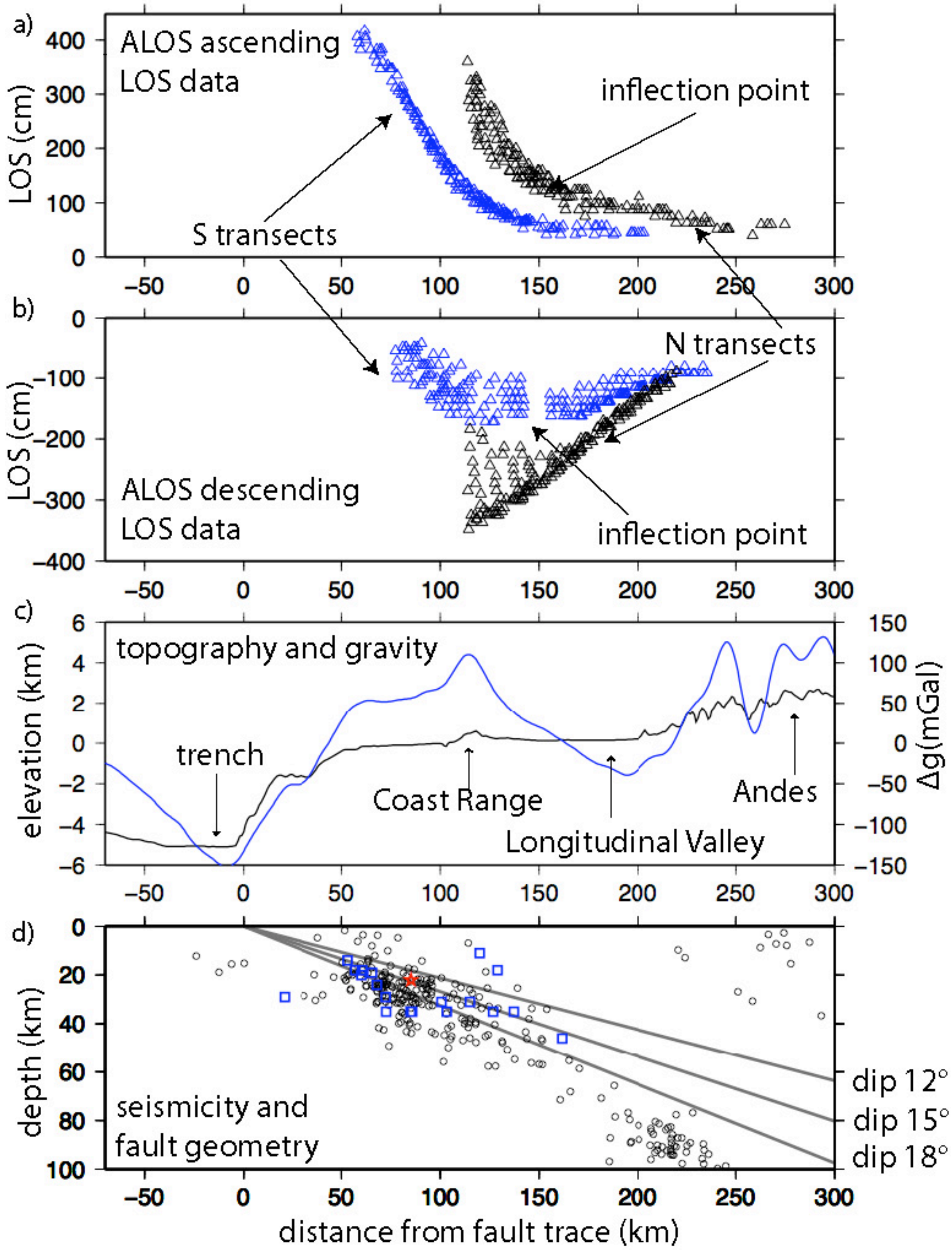

185

186 Figure S2. Transects of unwrapped line-of-sight data a) ascending and b) descending.
187 Locations of north (black) and south (blue) transects are shown in Figure S1. c)
188 Topography (black line) and free-air gravity (blue line) profiles over Chile illustrate the
189 major geological features. d) Seismicity and fault geometry. The black circles show the
190 background seismicity, the red star shows the epicenter, and the blue squares show the

locations of the M>6 aftershocks from the PDE catalog [*NEIC*, 2010].

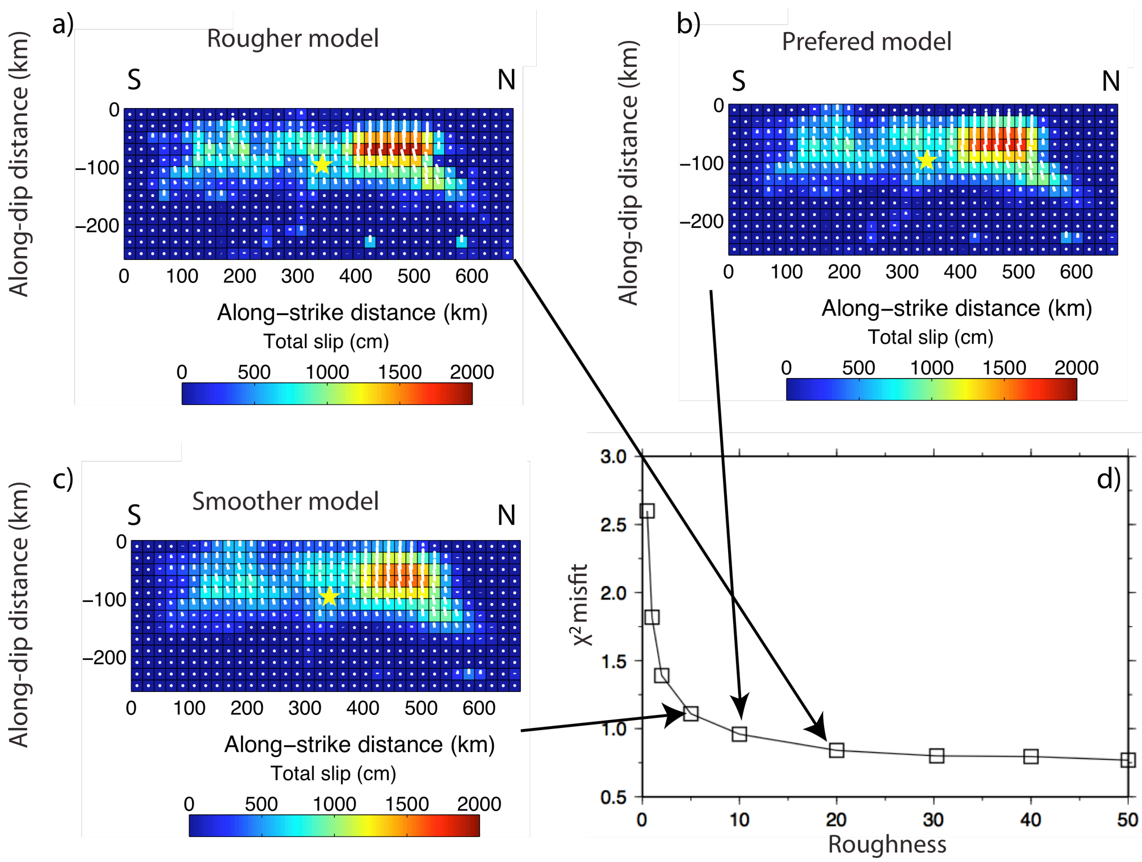

Figure S3. Slip models with three different weights on the smoothing function. The total slip magnitude on fault patches are represented by the color. In each slip model, the white lines, which originate from center of the rectangular patches and point outward, illustrate the relative motion of the hanging wall with respect to the footwall (mainly thrust slip with small right-lateral strike slip in this case). The yellow star is the position of the main shock. a) A rougher model. b) Our preferred model. c) A smoother model. d) The trade-off curve showing the χ^2 misfit versus the roughness.

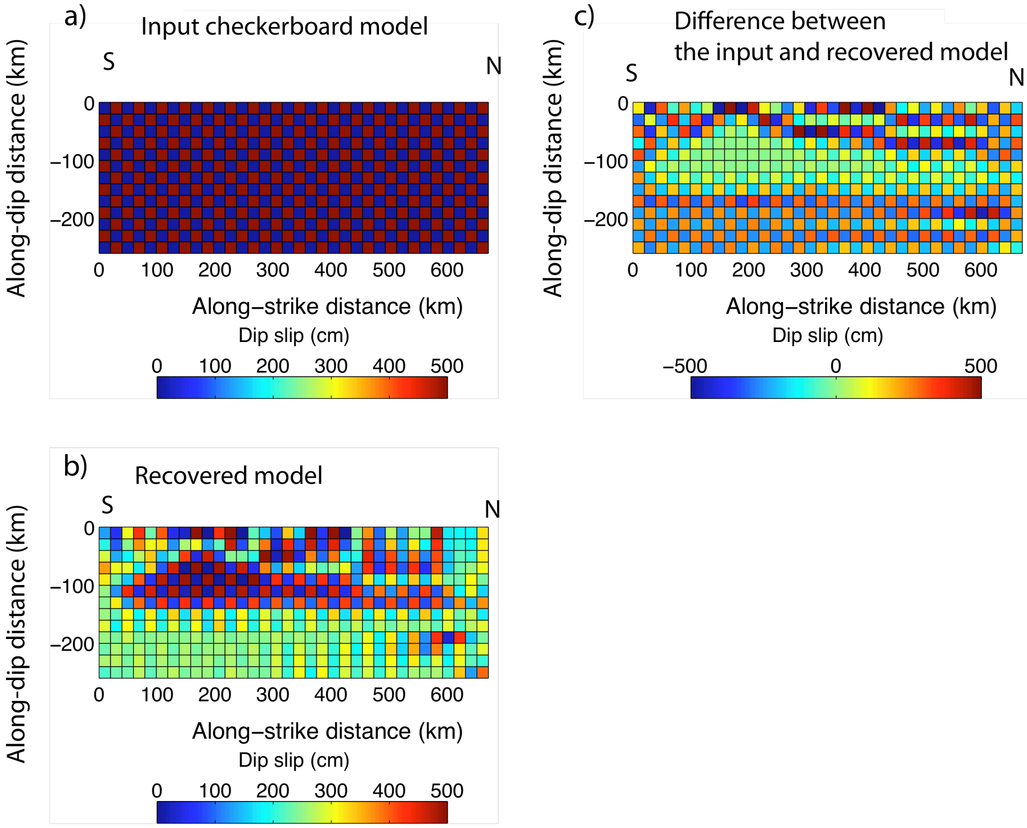

Figure S4. Resolution test with checker size of 20 km. a) Synthetic input model has thrust displacement of either zero or 500 cm spaced at 20 km intervals . b) The recovered model. c) The difference between the synthetic input model and the recovered model.

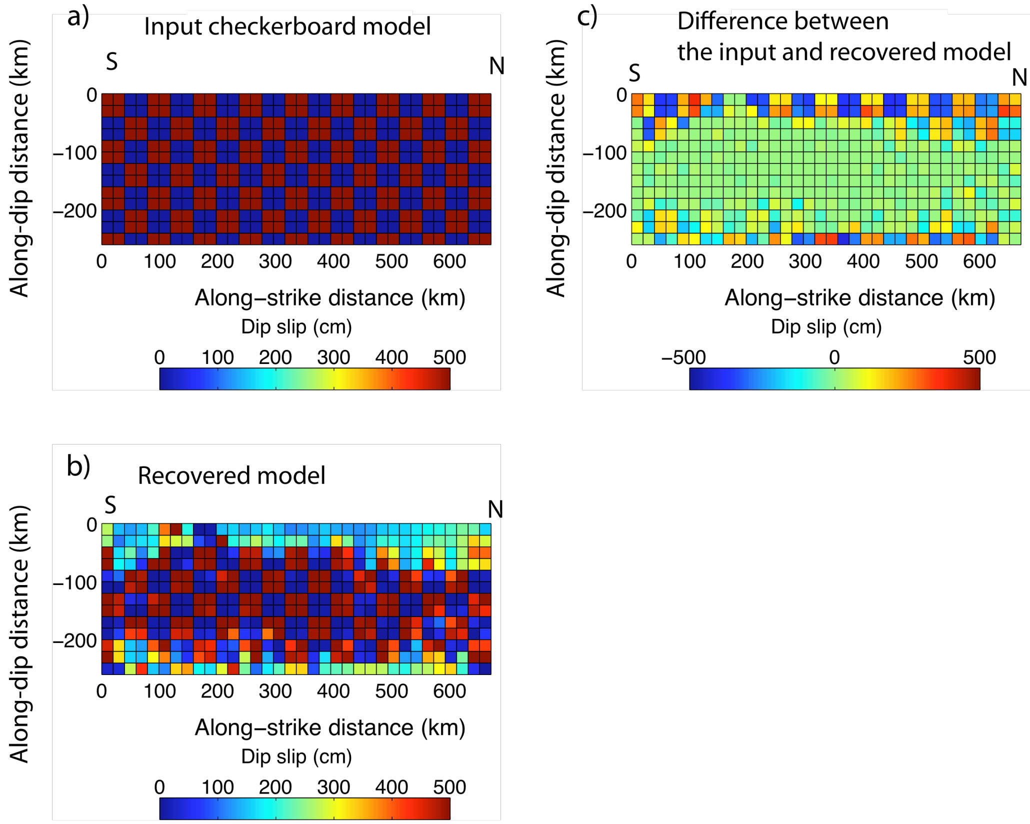

Figure S5. Resolution tests with checker size of 40 km. a) Synthetic input model that has thrust displacement of either zero or 500 cm spaced at 40 km intervals. b) The recovered model. c) The difference between the synthetic input model and the recovered model.

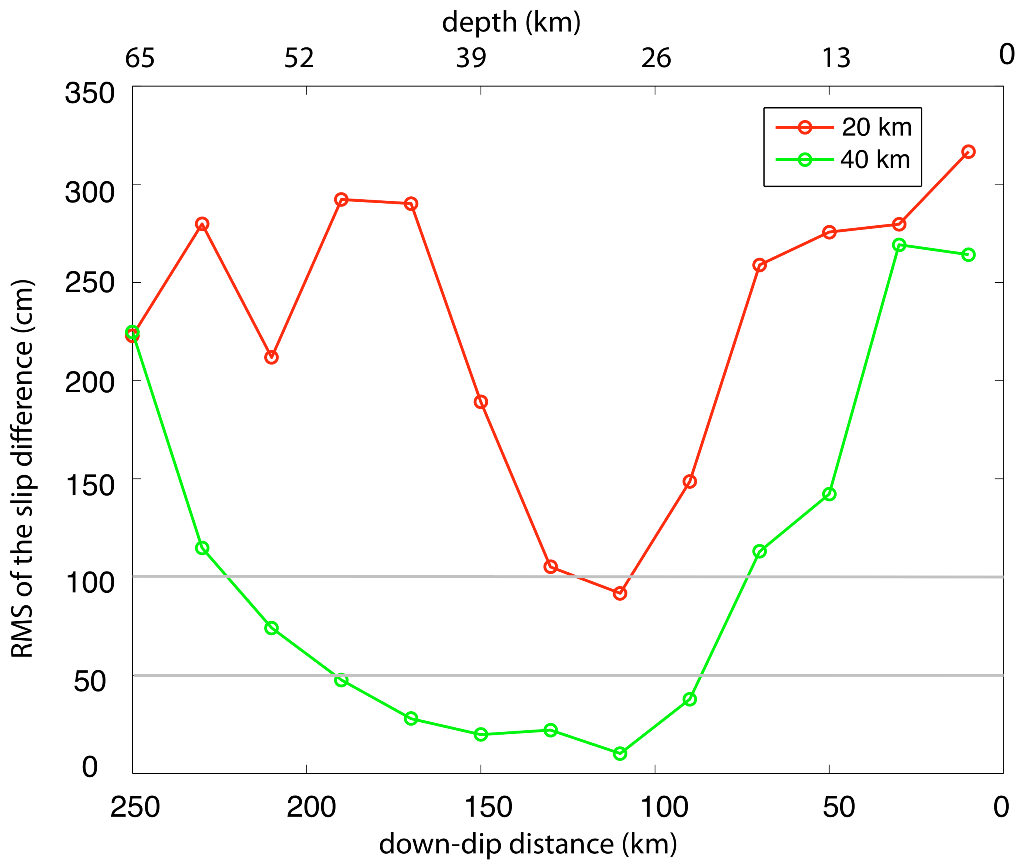

Figure S6. Accuracy of slip recovery versus downdip distance for 20 km (red line) and 40 km (green line) checker sizes. The RMS slip difference is the along-strike average of slip differences shown in Figure S4 (red line) and Figure S5 (green line). The horizontal axis shows the downdip distance (below) and depth (above). We set 20% RMS of the slip difference as the accuracy threshold so in this case the model is resolved at 20 km between downdip distances of 110 and 130 km and the model is resolved at 40 km between downdip distances of 70 and 220 km.

Table S1. GPS measurements used in this study and their fits to the model.

name	longitude	latitude	east displacement (cm)		north displacement (cm)		up displacement (cm)	
			data	model	data	model	data	model
ANTC	-71.532	-37.338	-80.62 ± 0.41	-81.62	18.37 ± 0.35	17.90	-2.73 ± 1.22	-5.48
CONZ	-73.025	-36.843	-300.19 ± 1.49	-300.15	-67.76 ± 1.33	-67.89	-3.98 ± 2.04	-4.28
MZ04	-69.020	-32.948	-12.17 ± 0.51	-15.20	-4.93 ± 0.32	-5.68	1.89 ± 1.13	-1.20
SANT	-70.668	-33.150	-23.53 ± 1.46	-25.19	-14.07 ± 1.12	-14.24	-1.76 ± 1.88	-5.88
LNQM	-71.361	-38.455	-33.44 ± 0.57	-34.67	14.31 ± 0.42	14.32	0.47 ± 1.34	-3.85
MZ05	-69.169	-32.951	-12.63 ± 0.53	-15.77	-5.19 ± 0.32	-6.15	1.79 ± 1.04	-1.46
ACPM	-70.537	-33.447	-41.49 ± 0.51	-40.24	-18.55 ± 0.33	-18.20	-1.90 ± 1.07	-5.96
BAVE	-70.765	-34.167	-116.61 ± 0.17	-116.57	-19.49 ± 0.17	-19.49	-9.44 ± 0.67	-9.94
LAJA	-71.376	-37.385	-72.18 ± 0.45	-71.77	17.77 ± 0.34	17.65	-2.36 ± 1.31	-5.00
LLFN	-71.788	-39.333	-11.20 ± 0.41	-12.53	7.86 ± 0.35	7.69	-1.74 ± 1.13	-3.66
LNDS	-70.575	-32.839	-14.27 ± 0.42	-15.38	-9.50 ± 0.17	-9.34	-1.53 ± 1.00	-4.83
MOCH	-73.904	-38.410	-120.39 ± 0.77	-120.36	-29.45 ± 0.40	-29.45	20.29 ± 1.28	20.27
NIEB	-73.401	-39.868	-0.49 ± 0.55	-1.76	-2.90 ± 0.46	-3.67	-1.26 ± 1.25	-4.43

Table S2: InSAR data used in this study.

track ID	orbit ID reference/repeat	acquisition dates reference/repeat[a]	perpendicular baseline[b] (m)	frames	observation mode	comments
ascending tracks						
T111	07119/21881	5/27/07--3/4/2010	215	6480--6520	FBS-FBS	
T112	21458/22129	2/3/10--3/21/2010	485	6470--6500	FBS-FBS	propagation phase delay
T113	10970/21706	2/15/08--4/7/2010	274	6470-6500	FBS-FBS	more recent pair is noisy
T114	21283/21954	1/22/10--3/9/10	284	6460--6480	FBS-FBS	
T115	21531/22202	2/8/10--5/11/2010	409	6470	FBS-FBS	PRF change[c]
T116	21779/22450	2/25/2010--4/12/10	480	6460	FBS-FBS	propagation phase delay
T117	09949/22027	12/7/07--3/14/10	157	6420-6440	FBS-FBS	low coherence
T118	21604/22275	2/13/2010--3/31/10	717	6410--6430	FBS-FBS	
T119	21181/21852	1/15/10--3/2/10	453	6400--6420	FBS-FBS	
descending tracks						
T422-sw3	11779/21844	4/10/08--3/1/10	1411	4350	ScanSAR-ScanSAR[d]	low coherence
T422-sw4	21173/21844	1/14/10--3/1/2010	560	4300-4400	FBS-ScanSAR[e]	
T420	21348/22019	1/26/10--3/13/2010	517	4330-4400	FBS-FBS	

[a] short time span (i.e., one orbit cycle) between reference and repeat passes is preferred to measure coseismic deformation
[b] short perpendicular baseline is preferred to remove topography phase noise
[c] PRF means Pulse Repetition Frequency
[d] See text for details
[e] See text for details

Table S3. Shear modulus structure in Maule, Chile region [after *Bohm et al*., 2002].

depth (km)	V_p (km/s)	V_s (km/s)	density (kg/m^3)	shear modulus (GPa)
-2 - 0	4.39	2.4	2100	12.1
0 - 5	5.51	3.19	2600	21.4
5 - 20	6.28	3.6	2800	36.3
20 - 35	6.89	3.93	2800	43.2
35 - 45	7.4	4.12	2800	47.5
45 - 55	7.76	4.55	3300	68.3
55 - 90	7.94	4.55	3300	68.3
90 - ∞	8.34	4.77	3300	75.1